

Cite this: *RSC Appl. Interfaces*, 2026, 3, 384Received 2nd September 2025,  
Accepted 8th January 2026

DOI: 10.1039/d5lf00258c

rsc.li/RSCApplInter

# Pseudocapacitive enhancement of VACNTs with SnO<sub>2</sub> for next-generation supercapacitors

Chinaza E. Nwanno,<sup>a</sup> Arun Thapa,<sup>a</sup> John Watt,<sup>b</sup> Winson Kuo<sup>b</sup> and Wenzhi Li<sup>\*,a</sup>

Developing high-performance supercapacitors requires electrode materials that combine high energy density, rapid charge transport, and long-term stability. In this study, we report a binder-free hybrid SnO<sub>2</sub>/vertically aligned carbon nanotubes (VACNTs) composite electrode by directly growing VACNTs on nickel foam *via* a plasma-enhanced chemical vapor deposition (PECVD) technique, followed by uniform SnO<sub>2</sub> nanoparticles coating through a wet-chemical method. The hierarchical structure integrates the electric double-layer capacitance (EDLC) of VACNTs with the pseudocapacitance of SnO<sub>2</sub>, resulting in enhanced electrochemical performance. The SnO<sub>2</sub>/VACNTs electrode exhibited a high specific capacitance (262.39 F g<sup>-1</sup> at 5 mV s<sup>-1</sup>) in 1 M KOH, significantly exceeding pristine VACNTs (24.02 F g<sup>-1</sup>). It delivered an energy density of 22.79 W h kg<sup>-1</sup> at a power density of 0.18 kW kg<sup>-1</sup> and retained 93% of its initial capacitance after 2000 cycles, demonstrating excellent rate capability and stability. Electrochemical impedance spectroscopy (EIS) revealed a low charge-transfer resistance (0.93 Ω) and small equivalent series resistance (1.65 Ω), indicating efficient electron and ion transport through the conductive VACNT framework. These results highlight the potential of SnO<sub>2</sub>/VACNTs composites as promising binder-free electrodes for next-generation high-energy, high-power supercapacitors.

## 1. Introduction

The growing demand for efficient, sustainable, and high-performance energy storage systems has driven intensive research into materials that can deliver both high energy and power densities. Among various technologies such as Zn-air batteries,<sup>1,2</sup> lithium-ion batteries,<sup>3,4</sup> and others, electrochemical supercapacitors have attracted particular attention as promising alternatives that effectively bridge the gap between conventional capacitors and batteries.<sup>5,6</sup> They offer higher energy density than traditional capacitors<sup>7</sup> and higher power density than batteries,<sup>8,9</sup> making them ideal for applications requiring rapid charge-discharge and long-term stability. Supercapacitors store energy through two primary mechanisms: (i) Electric double-layer capacitors (EDLCs), where energy is stored *via* charge separation at the electrode-electrolyte interface,<sup>10-13</sup> and (ii) pseudocapacitors, which utilize transition metal oxides and conducting polymers that undergo reversible Faradaic redox reactions.<sup>14-18</sup>

Carbon-based materials such as activated carbon,<sup>19-23</sup> xerogels,<sup>24-27</sup> aerogels,<sup>28-32</sup> mesoporous carbon,<sup>33-37</sup> carbon nanotubes (CNTs),<sup>38-42</sup> and graphene (G)<sup>43-48</sup> are widely used

in EDLCs due to their high conductivity, structural stability,<sup>49</sup> and large surface area.<sup>50</sup> Vertically aligned carbon nanotubes (VACNTs) are particularly attractive due to their structural and physical properties, including high electrical conductivity, excellent mechanical strength, and well-organized pores, which facilitate efficient charge transport and rapid ion diffusion.<sup>51,52</sup> Unlike randomly oriented CNTs, VACNTs provide direct pathways for ion movement, minimizing internal resistance and improving rate capability.<sup>3</sup> Despite these advantages, pristine VACNTs exhibit relatively low specific capacitance, limiting their energy storage potential. Previous studies on pristine VACNT-based supercapacitors have reported low specific capacitance values. For example, Ghai *et al.*<sup>53</sup> reported low specific capacitance of ~3.01 F g<sup>-1</sup> for VACNTs grown on aluminum (Al) foil, while Moreno *et al.*<sup>54</sup> observed a specific capacitance of 44 F g<sup>-1</sup> for untreated VACNTs synthesized on stainless steel (SS), demonstrating the limited charge storage capability of pure VACNTs as EDLC electrodes. This limitation arises from the fact that energy storage in pristine carbon-based materials like VACNTs is based solely on electrostatic charge accumulation, lacking any faradaic contribution to increase capacitance.

To overcome this drawback, researchers have explored hybrid electrode architectures, incorporating pseudocapacitive transition metal oxides such as manganese oxide (MnO<sub>2</sub>), nickel oxide (NiO), cobalt oxide (Co<sub>3</sub>O<sub>4</sub>) and

<sup>a</sup> Department of Physics, Florida International University, Miami, FL, 33199, USA.  
E-mail: Wenzhi.Li@fiu.edu

<sup>b</sup> Center for Integrated Nanotechnologies, Los Alamos National Laboratory, Los Alamos, NM, 87545, USA



tin oxide (SnO<sub>2</sub>), *etc.*, into carbon nanostructures like CNTs, graphene, carbon (C), and carbon nanofibers (CNF), to enhance electrochemical performance. These transition metal oxides can directly store a large amount of energy due to their ability to undergo rapid surface redox reactions involving ion adsorption and desorption coupled with electron transfer.<sup>55</sup> Among various metal oxides, SnO<sub>2</sub> has been widely investigated due to its low cost, non-toxicity, high theoretical capacitance, and ability to operate over a broad potential window. In addition, SnO<sub>2</sub> possesses a low electron chemical potential, which facilitates fast redox reactions, making it an ideal candidate for supercapacitor electrode applications.<sup>56</sup> Studies have demonstrated the improved electrochemical performance of SnO<sub>2</sub>-based carbon composites. For instance, Li *et al.*<sup>57</sup> fabricated SnO<sub>2</sub>/SWCNTs core-shell nanowires by the electrodeposition of the SnO<sub>2</sub> nanoparticles on the single-walled carbon nanotubes (SWCNTs), achieving a high specific capacitance of ~320 F g<sup>-1</sup> at 6 mV s<sup>-1</sup>, which was significantly higher than that of the pristine SWCNTs (~135 F g<sup>-1</sup>). Similarly, Vinoth *et al.*<sup>58</sup> reported a specific capacitance of 133.33 F g<sup>-1</sup> for an SnO<sub>2</sub>-decorated multiwalled carbon nanotubes (MWCNTs) electrode fabricated using a sonochemical procedure. Kuok *et al.*<sup>59</sup> developed a screen-printed SnO<sub>2</sub>/CNT quasi-solid-state supercapacitor that exhibited an areal capacitance of 5.61 mF cm<sup>-2</sup> when flat and 5.68 mF cm<sup>-2</sup> under bending, with an impressive 96% capacitance retention after 1000 charge-discharge cycles.

Beyond CNT-based composites, researchers have also explored other carbon-SnO<sub>2</sub> hybrid electrodes, such as SnO<sub>2</sub>/CNFs, SnO<sub>2</sub>/C, and SnO<sub>2</sub>/G composites. For example, Samuel *et al.*<sup>60</sup> fabricated core-shell SnO<sub>2</sub>/CNF composite mats *via* a single-nozzle one-step electrospinning method, achieving a high specific capacitance of 289 F g<sup>-1</sup> at a scan rate of 10 mV s<sup>-1</sup> and capacitance retention of 88% after 5000 cycles. Rani *et al.*<sup>115</sup> reported a high specific capacitance of 432 F g<sup>-1</sup> at a current density of 1 A g<sup>-1</sup> and capacitance retention of 95% after 2000 cycles for an SnO<sub>2</sub>@C composite from porous polymer beads by impregnation method. Additionally, Lim *et al.*<sup>61</sup> synthesized SnO<sub>2</sub>/graphene nanocomposites using a solvothermal approach, achieving a significantly enhanced specific capacitance of 363.3 F g<sup>-1</sup>, which was nearly five times higher than that of pristine graphene (68.4 F g<sup>-1</sup>). The superior electrochemical performance was attributed to the synergistic effect between the highly conductive graphene sheets and the pseudocapacitive SnO<sub>2</sub> nanoparticles, which improved charge storage and transport efficiency. Similarly, Jin *et al.*<sup>116</sup> fabricated a graphene-SnO<sub>2</sub>-polyaniline (GSP) ternary composite *via* a one-pot method, reporting an exceptional specific capacitance of 913.4 F g<sup>-1</sup> at 5 mV s<sup>-1</sup>, with a capacitance retention of 90.8% after 1000 cycles. The remarkable performance of the GSP composite was attributed to the combined advantages of graphene's conductivity, the pseudocapacitive contribution of SnO<sub>2</sub>, and polyaniline's additional faradaic reactions.

However, despite extensive studies on SnO<sub>2</sub>/CNT, SnO<sub>2</sub>/C, and SnO<sub>2</sub>/G, no prior research has investigated the use of SnO<sub>2</sub>/VACNTs composites as supercapacitor electrodes. Unlike randomly oriented CNTs, VACNTs provide a vertically aligned structure that enhances ion accessibility and electron transport efficiency, potentially addressing the diffusion limitations of metal-oxide-based electrodes. By leveraging the synergistic combination of high conductivity of VACNTs and the pseudocapacitive behavior of SnO<sub>2</sub>, a SnO<sub>2</sub>/VACNTs composite electrode can deliver superior electrochemical performance, including higher specific capacitance, improved energy and power densities, and lower charge transfer resistance.

In this study, VACNTs were synthesized directly on nickel (Ni) foam substrates using the plasma-enhanced chemical vapor deposition (PECVD) technique, providing a robust, binder-free electrode structure with excellent electrical connectivity. A wet chemical method<sup>62</sup> was used to coat the SnO<sub>2</sub> nanoparticles onto the VACNT array, forming a composite electrode that integrates EDLC and pseudocapacitive charge storage mechanisms. Electrochemical characterization revealed that the SnO<sub>2</sub>/VACNTs composite exhibits high specific capacitance, excellent rate capability, and impressive cycling stability. The work represents the first systematic investigation of SnO<sub>2</sub>/VACNTs as a supercapacitor electrode, offering new insights into developing high-performance hybrid energy storage materials.

## 2. Experimental methods

### 2.1. Electrodes preparation

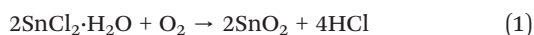
**2.1.1. VACNTs synthesis.** VACNTs were directly grown on Ni foams (99.99 wt%, Alfa Aesar) using a PECVD technique. Before the growth process, the Ni foams were cut into 1 cm × 1 cm squares and cleaned *via* ultrasonication in acetone and isopropyl alcohol (IPA) for 10 minutes each, followed by air drying. The cleaned Ni substrates were then loaded into the PECVD system for VACNT synthesis. The reaction chamber was initially evacuated to a base pressure of 0.01 Torr, and ammonia (NH<sub>3</sub>) gas was introduced at a flow rate of 195 sccm, maintaining a chamber pressure of 7 Torr. The temperature was ramped up to 700 °C at a rate of 50 °C min<sup>-1</sup> under NH<sub>3</sub> atmosphere, where NH<sub>3</sub> acted as an etchant and reducing agent to remove surface oxides and contaminants from the Ni foam. This treatment promoted the formation of nanoscale Ni catalyst particles on the Ni foam surface through controlled surface roughening and reduction, thereby creating uniformly distributed active sites for CNT nucleation. The *in situ* formed Ni catalyst particles ensured good adhesion of the VACNTs to the Ni foam substrate. Upon reaching the desired growth temperature, a direct current (DC) plasma was initiated at 80 W, and acetylene (C<sub>2</sub>H<sub>2</sub>) gas was introduced at a flow rate of 35 sccm as the carbon precursor. Growth was conducted at a controlled total pressure of 7 Torr, maintained and



monitored using a throttle valve to ensure process stability and uniform plasma conditions. The VACNT synthesis proceeded for 15 minutes, after which the heating system, the plasma, and the gas flow were turned off, and the system was allowed to cool to room temperature at the base pressure before retrieving the samples from the system. The Ni foams were weighed before and after the growth procedure to ascertain the mass of VACNT deposition.

**2.1.2. SnO<sub>2</sub>/VACNTs composite fabrication.** The as-synthesized VACNTs on Ni foam were coated with a thin layer of SnO<sub>2</sub> nanoparticles using a wet-chemical method. Before coating, the VACNTs were treated with nitric acid (HNO<sub>3</sub>, 20 vol%) for 20 minutes to remove residual impurities and introduce oxygen-containing functional groups on the VACNT surface.<sup>63</sup> This functionalization step was essential for enhancing the hydrophilicity of the VACNTs, thereby promoting uniform SnO<sub>2</sub> coating over the entire length of the VACNTs.<sup>64</sup> The precursor solution was prepared by dissolving 1 g of tin(II) chloride (SnCl<sub>2</sub>, 98%, anhydrous, Alfa Aesar) in 80 mL of deionized (DI) water, followed by the addition of 1.4 mL of hydrochloric acid (HCl, 38%) to prevent the formation of tetratin hexahydroxide dichloride (Sn<sub>4</sub>(OH)<sub>6</sub>Cl<sub>2</sub>) colloidal particles, which could otherwise lead to the unintended formation of SnO instead of SnO<sub>2</sub> nanoparticles.<sup>65</sup>

Following the acid treatment, the VACNTs were thoroughly rinsed five times with DI water until the rinse solution reached a neutral PH (~7), confirming the complete removal of residual acidic species before immersion in the SnO<sub>2</sub> precursor solution. The solution was stirred with a constant and gentle air flow during the coating process to ensure uniform coating. The reaction proceeded at room temperature for a coating duration of 9 hours according to eqn (1) below:<sup>66</sup>



After the coating duration, the coated sample was rinsed thoroughly with DI water and dried at 95 °C for 12 hours. The mass loading of the SnO<sub>2</sub>/VACNTs composite was ~0.5 mg cm<sup>-2</sup> after drying. This was determined gravimetrically from the weight difference of the Ni foam before VACNT growth and after SnO<sub>2</sub> deposition, using a microbalance with ±0.01 mg accuracy. The coating mechanism was primarily governed by electrostatic interaction, where the positively charged Sn<sup>2+</sup> ions in the aqueous SnCl<sub>2</sub> solution were anchored onto the negatively charged functional groups on the VACNT surface.<sup>67</sup> This is followed by the *in situ* oxidation of the Sn<sup>2+</sup> cations to form SnO<sub>2</sub> nanoparticles.

**2.1.3. Structural and physical characterization.** Morphological analyses of the materials were conducted using field emission scanning electron microscopy (FE-SEM, JEOL JSM-6330F) and transmission electron microscopy (TEM, JEOL JEM 2100) operated at 300 kV. The nanostructure, elemental composition, and crystallinity of the various electrodes were further investigated using a

Tecnai F30 transmission electron microscopy (TEM) operated at 300 kV. To evaluate the thermal stability and composition, thermogravimetric analysis (TGA) was performed using a TG/DSC system (SDT Q600 V20.9, USA). The TGA analysis was conducted in airflow up to 900 °C at a heating rate of 10 °C min<sup>-1</sup>. Before TGA measurements, SnO<sub>2</sub>/VACNTs were detached from the Ni foam using an IPA ultrasonic bath for 10 min, followed by Ni residue removal with a strong bar magnet and overnight drying at 100 °C. The surface chemical composition and elemental states of the electrodes were analyzed using X-ray photoelectron spectroscopy (XPS, Omicron Nanotechnology, Oxford Instruments, Germany), equipped with a monochromatic Al-Kα (1486.6 eV) X-ray source operated at 15 kV and 20 mA. Binding energy calibration was performed using the C1s peak (284.6 eV). XPS data were deconvoluted using Origin 8.0 software to analyze chemical states and bonding configurations. The crystal structure and defect analysis of the pristine VACNTs and the SnO<sub>2</sub>-VACNTs composite were done using X-ray diffraction (Siemens Diffractometer D5000) with Cu Kα radiation (λ = 1.54 Å), a step size of 0.02°, a scanning range of 20–80°, and a speed of 2° min<sup>-1</sup>. Additionally, Raman spectroscopy was conducted using an Ar<sup>+</sup> laser with a wavelength of 632.8 nm. The presence of functional groups in the VACNTs and SnO<sub>2</sub>/VACNTs composites was further assessed using Fourier transform infrared spectroscopy (FTIR, Jasco FTIR-4100).

**2.1.4. Electrochemical characterization.** The electrochemical performance of pristine VACNTs, and SnO<sub>2</sub>/VACNTs composite electrodes was evaluated using CHI660E electrochemical workstation (CH Instruments Inc., Texas) in a three-electrode setup with 1 M potassium hydroxide (KOH) as the electrolyte at room temperature. An Ag/AgCl electrode (1 M Na<sub>2</sub>SO<sub>4</sub>) was used as the reference electrode, while a platinum wire was used as the counter electrode. The as-synthesized materials grown on Ni foam were used as the working electrodes. Cyclic voltammetry (CV) experiments were carried out at various scan rates over a potential range of -0.7 to 0.2 V to analyze the charge storage of each electrode. Additionally, galvanostatic charge-discharge (GCD) tests were performed at different current densities within the same voltage range to assess the charge-discharge characteristics and rate capability. To investigate the cycling stability, each electrode was subjected to 2000 CV cycles at 10 mV s<sup>-1</sup> and the capacitance retention was observed. Electrochemical impedance spectroscopy (EIS) measurements were conducted in the 0.01 Hz to 50 kHz frequency range at a perturbation amplitude of 10 mV to analyze charge transfer resistance (*R*<sub>ct</sub>) and ion diffusion kinetics. Before conducting the electrochemical tests, at least 20 preliminary CV cycles at 50 mV s<sup>-1</sup> were run to stabilize the electrodes. Standard electrochemical equations were applied to determine and compare the specific capacitance, energy density, and power density of the different electrode materials.



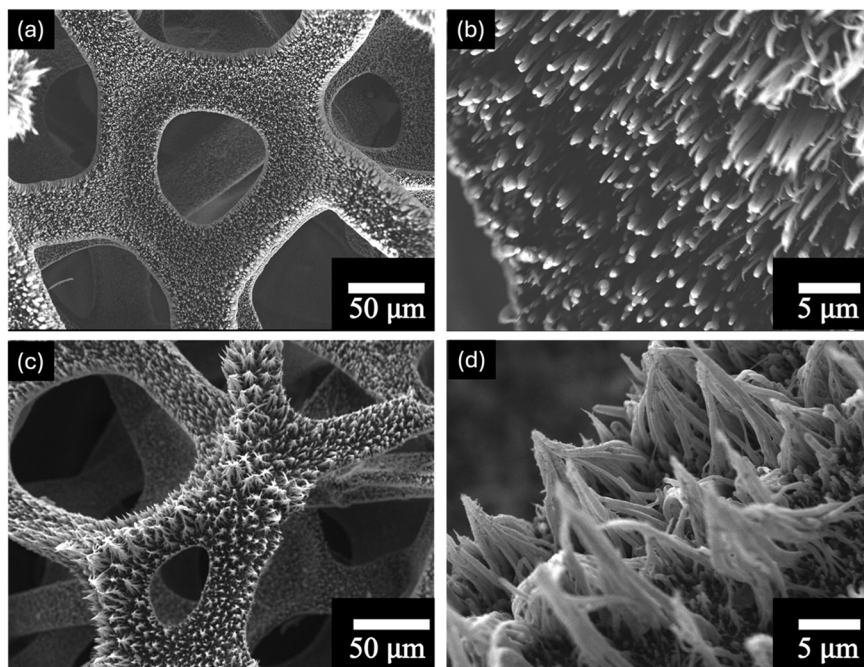


Fig. 1 SEM images of VACNTs before and after  $\text{SnO}_2$  coating. (a and b) Low and high-magnification SEM images of pristine VACNTs on Ni foam. (c and d) Low and high magnification SEM images of  $\text{SnO}_2$ -coated VACNTs.

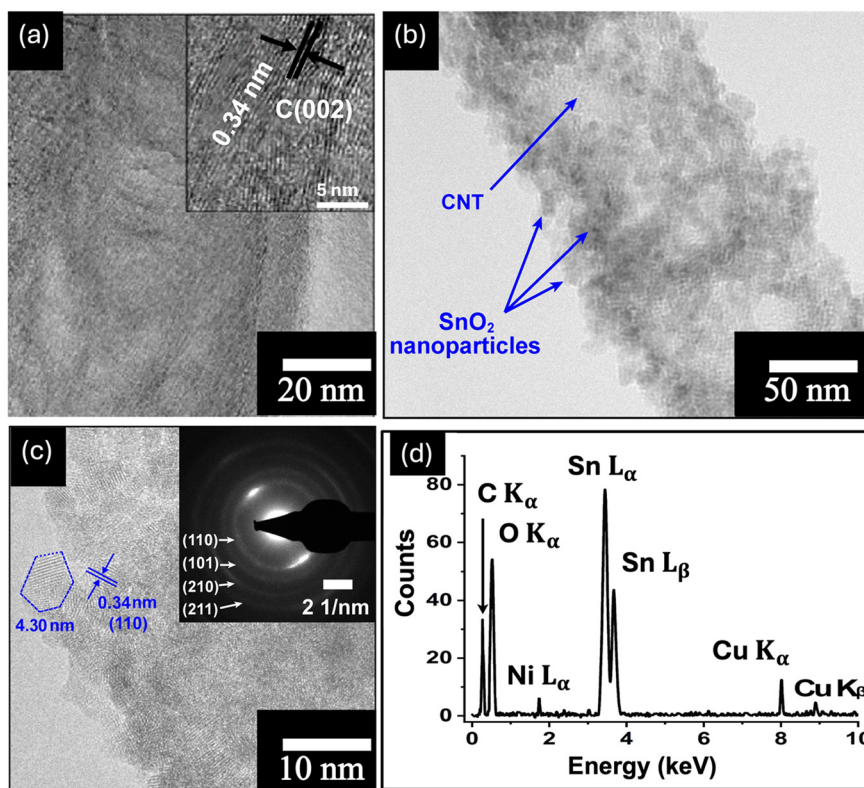


Fig. 2 TEM images of pristine VACNT and  $\text{SnO}_2$ /VACNT. (a) HRTEM image of a pristine VACNT with an inset showing a lattice of 0.34 nm, typical of MWCNTs. (b and c) HRTEM images of an  $\text{SnO}_2$ -VACNT, showing  $\text{SnO}_2$  nanoparticles uniformly distributed on the CNT surface and a lattice fringe of 0.34 nm, which corresponds to the (110) plane of  $\text{SnO}_2$ . The inset in (c) shows the SAED pattern, confirming the polycrystalline nature of  $\text{SnO}_2$ . (d) EDX spectrum of the  $\text{SnO}_2$ /VACNTs composite.



### 3. Results and discussion

#### 3.1. Structural and physical properties

The SEM images in Fig. 1 show the morphological evolution of the VACNTs before and after SnO<sub>2</sub> coating. The low-magnification image in Fig. 1(a) shows the pristine VACNTs directly grown on Ni foam, forming a well-defined porous network where the nanotubes maintain vertical alignment. The direct attachment of VACNTs to the Ni foam substrate is expected to provide a highly conductive pathway for electron transfer between the active material and the substrate, effectively reducing interfacial contact resistance, a crucial factor for high-rate charge/discharge performance. Additionally, the porous structure of the VACNT network enhances the accessible surface area, facilitates electrolyte penetration for efficient ion transport, and promotes uniform nanoparticles deposition.<sup>68,69</sup> When a poorly conductive material like SnO<sub>2</sub> is coated onto the VACNTs, the nanotubes will ensure efficient electron transfer between the SnO<sub>2</sub> nanoparticles and the Ni substrate, enhancing the overall electrochemical performance of the resulting composite electrode. The high-resolution image in Fig. 1(b) further corroborates the porous structure and the alignment of the VACNT array. Fig. 1(c) and (d) show the morphological changes of the as-synthesized VACNTs after SnO<sub>2</sub> coating. In Fig. 1(c), the low-magnification image shows that the overall porous network is maintained. However, noticeable bundling of the VACNTs occurs likely due to surface tension forces at the liquid-CNT interface during the SnO<sub>2</sub> coating process, leading to localized aggregation.<sup>70,71</sup> This bundling enhances mechanical stability,<sup>72,73</sup> making the SnO<sub>2</sub>/VACNTs composite a promising candidate for energy storage applications. The high-magnification image of the SnO<sub>2</sub>/VACNTs composite (Fig. 1(d)) provides a clearer view of the SnO<sub>2</sub> coating, confirming the bundled nature of the resulting SnO<sub>2</sub>/VACNTs composite. The image also reveals a roughened texture on the VACNTs surfaces, indicating successful SnO<sub>2</sub> coating across the entire lengths of the VACNTs.

The TEM images in Fig. 2 provide insight into the structural and crystallographic properties of the as-synthesized VACNTs and SnO<sub>2</sub>/VACNTs composite. Fig. 2(a) presents a high-resolution TEM (HRTEM) image of a pristine VACNT with an inset at the top right corner showing a well-defined lattice fringe with an interplanar spacing of 0.34 nm which corresponds to the characteristic spacing of multi-walled CNTs (MWCNTs).<sup>74</sup> This confirms the graphitic nature of the VACNTs before SnO<sub>2</sub> coating.<sup>75</sup> Fig. 2(b) shows SnO<sub>2</sub> nanoparticles distributed along the CNT surface, forming a conformal coating while maintaining the nanotube framework. This uniform coating of SnO<sub>2</sub> nanoparticles is beneficial for electrochemical applications, ensuring good interfacial contact for charge transfer.<sup>76</sup> Fig. 2(c) is the HRTEM image of the SnO<sub>2</sub>/VACNTs composite showing the crystalline nature of the SnO<sub>2</sub> nanoparticles, with a measured lattice fringe spacing of 0.34 nm, corresponding to the (110) plane of SnO<sub>2</sub> crystal. The polygonal feature marked in

Fig. 2(c) represents a crystalline grain measuring approximately 4.30 nm, indicating the nanostructured nature of the SnO<sub>2</sub> coating. The selected area electron diffraction (SAED) pattern in the inset reveals distinct diffraction rings indexed (110), (101), (210), and (211) planes, showing the polycrystalline nature of the SnO<sub>2</sub> nanoparticles. Fig. 2(d) shows the energy dispersive X-ray spectroscopy (EDX) spectrum of the SnO<sub>2</sub>/VACNTs, confirming the elemental composition of the composite. The strong peaks corresponding to Sn L<sub>α</sub> and Sn L<sub>β</sub> at approximately 3.4–4.0 keV indicate the successful deposition of SnO<sub>2</sub> nanoparticles onto the VACNTs. The presence of prominent C K<sub>α</sub> and O K<sub>α</sub> at low energy suggests the carbonaceous nature of the VACNTs and the oxygen content from the SnO<sub>2</sub>. The Ni L<sub>α</sub> is from the Ni foam substrate. Additionally, the Cu K<sub>α</sub> and Cu K<sub>β</sub> at around 8 keV stem from the copper grid used for TEM analysis.

The structural, compositional, and chemical characteristics of the SnO<sub>2</sub>/VACNTs composites, including X-ray diffraction (XRD), Raman spectroscopy, Fourier-transform infrared spectroscopy (FTIR), thermogravimetric analysis (TGA), and X-ray photoelectron spectroscopy (XPS) have been comprehensively reported in our previous work<sup>62</sup> (see Fig. S1 and S2). In brief, the XRD patterns (Fig. S1(a)) confirmed the presence of the tetragonal crystalline SnO<sub>2</sub> phase, while the Raman spectra (Fig. S1(b)) showed a slight increase in the I<sub>D</sub>/I<sub>G</sub> ratio (from 1.12 to 1.18) after SnO<sub>2</sub> coating, indicating defect formation due to HNO<sub>3</sub> treatment. These defects play a significant role in enhancing electrochemical performance. Surface defects such as vacancies, dangling bonds, edge dislocations, and functional groups can act as additional active sites for ion adsorption, thereby contributing to increased charge storage capacity.<sup>77,78</sup> Moreover, these defect sites can facilitate faster ion transport by reducing the energy barriers for ion diffusion at the electrode–electrolyte interface.<sup>79</sup> Consequently, the presence of such defects in the VACNTs network is expected to enhance both the capacitive behavior and the overall electrochemical performance of the SnO<sub>2</sub>/VACNTs electrode. FTIR analysis (Fig. S1(c)) revealed the emergence of oxygen-containing functional groups (C=O, –OH, C–O) on VACNT surfaces, which facilitated uniform SnO<sub>2</sub> coating. TGA (Fig. S1(d)) revealed that the composite retained approximately 40 wt% SnO<sub>2</sub> and remained thermally stable up to 800 °C. XPS wide-survey spectrum result (Fig. S2(a)) confirmed the presence of Sn, O, and C elements, consistent with successful SnO<sub>2</sub> coating on the VACNT framework. The Sn 3d core-level spectrum (Fig. S2(b)) exhibited two distinct peaks at approximately 487.7 eV (Sn 3d<sub>5/2</sub>) and 496.2 eV (Sn 3d<sub>3/2</sub>), characteristic of Sn<sup>4+</sup> species in tetragonal SnO<sub>2</sub>, with no evidence of lower oxidation states. The deconvoluted O 1s spectrum (Fig. S2(c)) showed components at 531.3 eV, 532.0 eV, and 533.5 eV, corresponding to O–Sn, O=C, and O–C=O functional groups.<sup>80,81</sup> Meanwhile, the C 1s profile (Fig. S2(d)) displayed peaks at 284.9 eV, 285.7 eV, 287.4 eV, and 290.2 eV, which correspond to C–C, O–C, C=O, and O=C–O



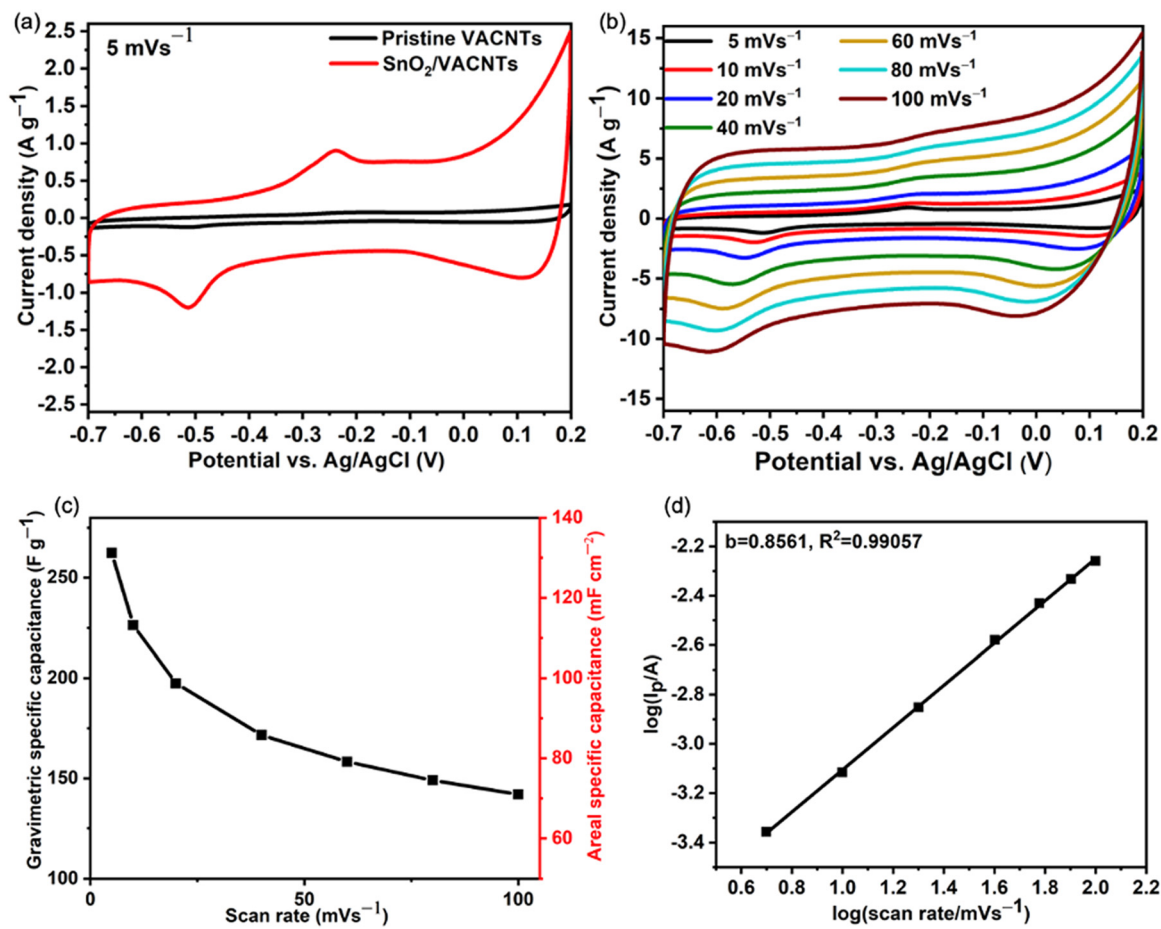


Fig. 3 (a) CV curves of the pristine VACNTs and SnO<sub>2</sub>/VACNTs electrodes at a fixed scan rate of 5 mV s<sup>-1</sup>. (b) CV curves of the SnO<sub>2</sub>/VACNTs composite electrode at different scan rates. (c) Variation of gravimetric and areal specific capacitances of the SnO<sub>2</sub>/VACNTs electrode. (d) Graph of log of peak current (*I*<sub>p</sub>) vs. log of scan rate (*v*).

functional groups, respectively.<sup>82,83</sup> These results confirm that the SnO<sub>2</sub> layer is chemically well integrated with the VACNT network, promoting strong interfacial coupling beneficial for charge transfer in electrochemical processes.

### 3.2. Electrochemical performance studies

The electrochemical performance of the pristine VACNTs and SnO<sub>2</sub>/VACNTs electrodes was evaluated using CV. Fig. 3(a)

**Table 1** Comparison of the electrochemical performance of the pristine VACNTs and the SnO<sub>2</sub>/VACNTs composite with results reported in the literature using similar materials

Electrode	Synthesis method	Scan rate/current density	Potential window (V)	Specific capacitance (F g <sup>-1</sup> )	Electrolyte	Capacitance retention (%)	Ref.
Aligned CNTs	CVD	100 mV s <sup>-1</sup>	0–2.5	23.8	—	—	100
CNT sheet	CVD	0.1 A g <sup>-1</sup>	0–0.8	19.2	PVA	—	101
VACNTs	ICVD	1 A g <sup>-1</sup>	0.2–0.8	75	1 M H <sub>2</sub> SO <sub>4</sub>	84 after 1000 cycles	69
VACNTs	TCVD	50 mV s <sup>-1</sup>	0–0.8	3.01	1 M Na <sub>2</sub> SO <sub>4</sub>	—	53
SnO <sub>2</sub> /C	Chemical	5 mV s <sup>-1</sup>	0–1.0	37.8	1 M H <sub>2</sub> SO <sub>4</sub>	—	84
SnO <sub>2</sub> /C	Chemical	2 A g <sup>-1</sup>	-0.4–0.6	150	4.5 M H <sub>2</sub> SO <sub>4</sub>	>90 after 2000 cycles	102
SnO <sub>2</sub> /carbon aerogel	Sol-gel	10 mA g <sup>-1</sup>	-1.0–1.0	69.8	1 M H <sub>2</sub> SO <sub>4</sub>	—	103
SnO <sub>2</sub> /CNF	Electrospinning	1 A g <sup>-1</sup>	0–1.0	118	1 M H <sub>2</sub> SO <sub>4</sub>	94.6 after 10 000 cycles	96
SnO <sub>2</sub> /CNFs	Electrospinning	20 mVs <sup>-1</sup>	-0.2–0.9	187	1 M H <sub>2</sub> SO <sub>4</sub>	95 after 1000 cycles	81
SnO <sub>2</sub> /graphene	Chemical	0.2 A g <sup>-1</sup>	-0.2–0.8	126	1 M H <sub>2</sub> SO <sub>4</sub>	98.2 after 2000 cycles	104
SnO <sub>2</sub> /graphene	Chemical	1 A g <sup>-1</sup>	0–1.0	184	6 M KOH	—	105
SnO <sub>2</sub> /MWCNT	Sonochemical	0.5 mA cm <sup>-2</sup>	0–1.0	133.33	1 M Na <sub>2</sub> SO <sub>4</sub>	—	58
SnO <sub>2</sub> /SWCNTs	Chemical	6 mV s <sup>-1</sup>	0–1.2	320	1 M Na <sub>2</sub> SO <sub>4</sub>	98 after 1000 cycles	57
VACNTs	PECVD	5 mV s <sup>-1</sup>	-0.7–0.2	24.02	1 M KOH	96 after 2000 cycles	This work
SnO <sub>2</sub> /VACNTs	Chemical	5 mV s <sup>-1</sup>	-0.7–0.2	262.39	1 M KOH	93 after 2000 cycles	This work



compares the CV curves of pristine VACNTs and SnO<sub>2</sub>/VACNTs at a constant scan rate of 5 mV s<sup>-1</sup>. The pristine VACNTs exhibit a nearly rectangular shape indicative of EDLC behavior, which is associated with carbon-based materials like CNTs, delivering a gravimetric specific capacitance of 24.02 F g<sup>-1</sup> (corresponding to an areal specific capacitance of 23.75 mF cm<sup>-2</sup>). On the other hand, the SnO<sub>2</sub>/VACNTs electrode exhibited a much higher gravimetric specific capacitance of 262.39 F g<sup>-1</sup> and a corresponding areal capacitance of 131.20 mF cm<sup>-2</sup>, showing distinct redox peaks, confirming the presence of faradaic reactions and pseudocapacitive charge storage arising from the redox activity of the SnO<sub>2</sub> nanoparticles on the surfaces of the VACNTs.<sup>84,85</sup> The enhanced charge storage capability of the SnO<sub>2</sub>/VACNTs composite can be attributed to a synergistic dual mechanism involving EDLC and pseudocapacitance. The VACNTs contribute to EDLC by enabling the electrostatic accumulation of electrolyte ions at the electrode–electrolyte interface, while the incorporation of SnO<sub>2</sub> introduces faradaic reactions, wherein charge is stored through fast, reversible redox reactions occurring at the electrode surface and near-surface regions. This performance surpasses several reported SnO<sub>2</sub>-based supercapacitor electrodes, including SnO<sub>2</sub>-graphene composites and SnO<sub>2</sub>-coated carbon fiber (SnO<sub>2</sub>/C), as shown in Table 1. Furthermore, the higher current density observed for the SnO<sub>2</sub>/VACNTs electrode compared to pristine VACNTs at the same scan rate indicates an enhanced charge storage capability attributed to the synergistic contributions from both the highly conductive VACNT framework and the electroactive SnO<sub>2</sub> nanoparticles. The faradaic reactions responsible for the pseudocapacitive behavior of the SnO<sub>2</sub> nanoparticles are given by the following equations:<sup>86</sup>

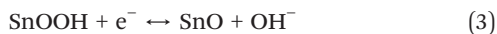


Fig. 3(b) shows the CV curves of the SnO<sub>2</sub>/VACNTs electrode at different scan rates ranging from 5 to 100 mV s<sup>-1</sup>. At lower scan rates, well-defined redox peaks are observed, confirming the pseudocapacitive behavior of the SnO<sub>2</sub> nanoparticles.<sup>87</sup> As the scan rate increases, the CV curves maintain a quasi-rectangular shape with noticeable redox peaks, indicating the presence of both EDLC and pseudocapacitive charge storage mechanisms. The retention of this shape across various scan rates is attributed to the alignment and well-defined porous structures of the VACNT array, which facilitates rapid ion transport and charge distribution, ensuring efficient electrochemical performance.<sup>88,89</sup> Although minor peak broadening and shifts occur at higher scan rates due to ion diffusion limitations, the composite electrode continues to exhibit stable capacitive behavior.

The specific capacitance as a function of scan rate is presented in Fig. 3(c). The gravimetric specific capacitance decreases from 262.39 F g<sup>-1</sup> at 5 mV s<sup>-1</sup> to 142.01 F g<sup>-1</sup> at 100

mV s<sup>-1</sup>, while the corresponding areal specific capacitance decreases from 131.20 mF cm<sup>-2</sup> to 71 mF cm<sup>-2</sup> over the same range. This decline is attributed to the limited diffusion of electrolyte ions into the inner active sites at higher scan rates, which restricts full utilization of the electrochemically accessible surface area.<sup>90,91</sup> At lower scan rates, the ions have sufficient time to penetrate the porous SnO<sub>2</sub>/VACNT network, allowing both surface adsorption and redox reactions to occur efficiently, thereby yielding higher capacitance values. Nevertheless, despite the decrease, the SnO<sub>2</sub>/VACNT composite retains a relatively high capacitance even at elevated scan rates, demonstrating excellent rate capability and efficient ion transport pathways within the VACNT structure. The gravimetric specific capacitance ( $C_{\text{grav}}$ ) and areal specific capacitance ( $C_{\text{areal}}$ ) at various scan rates were calculated from the following equations:<sup>86</sup>

$$C_{\text{grav}} = \frac{1}{m\nu\Delta V} \int I_{(\nu)} dV \quad (4a)$$

$$C_{\text{areal}} = \frac{1}{A\nu\Delta V} \int I_{(\nu)} dV \quad (4b)$$

where  $m$  is the mass of the pristine VACNTs, and the SnO<sub>2</sub>/VACNTs in grams (g),  $A$  is the geometric area of the electrodes (cm<sup>2</sup>),  $\nu$  is the scan rate,  $\Delta V$  is the sweep potential window and  $\int I_{(\nu)} dV$  is the integral area under the respective CV curves.

To gain insight into the charge-storage mechanism, the dependence of peak current ( $I_p$ ) on scan rate ( $\nu$ ) was analyzed using the power-law relation:

$$I_p = a\nu^b \quad (5a)$$

Taking logarithms gives.

$$\log(I_p) = \log(a) + b \log(\nu) \quad (5b)$$

where  $a$  is a proportionality constant related to the intrinsic electrochemical activity of the electrode, and  $b$  differentiates between capacitive ( $b \approx 1$ ) and diffusion controlled ( $b \approx 0.5$ ) processes.<sup>92</sup> As shown in Fig. 3(d), the slope of the  $\log(I_p)$  vs.  $\log(\nu)$  plot yields  $b = 0.856$  ( $R^2 = 0.9906$ ), indicating that charge storage in the SnO<sub>2</sub>/VACNTs electrode is predominantly surface-controlled with a minor diffusion contribution.<sup>93</sup>

The electrochemical performance of the electrodes was further evaluated from the charge–discharge profiles. Fig. 4(a) compares the GCD curves of the pristine VACNTs and SnO<sub>2</sub>/VACNTs at a constant current density of 0.5 A g<sup>-1</sup>. The pristine VACNTs exhibit a nearly symmetrical triangular charge–discharge profile, typical of an EDLC. In contrast, the SnO<sub>2</sub>/VACNTs electrode shows a longer charge–discharge duration and a deviation from the ideal triangular shape, indicating the presence of faradaic reactions associated with the pseudocapacitive behavior of SnO<sub>2</sub>. The specific capacitance values calculated from the discharge curves,



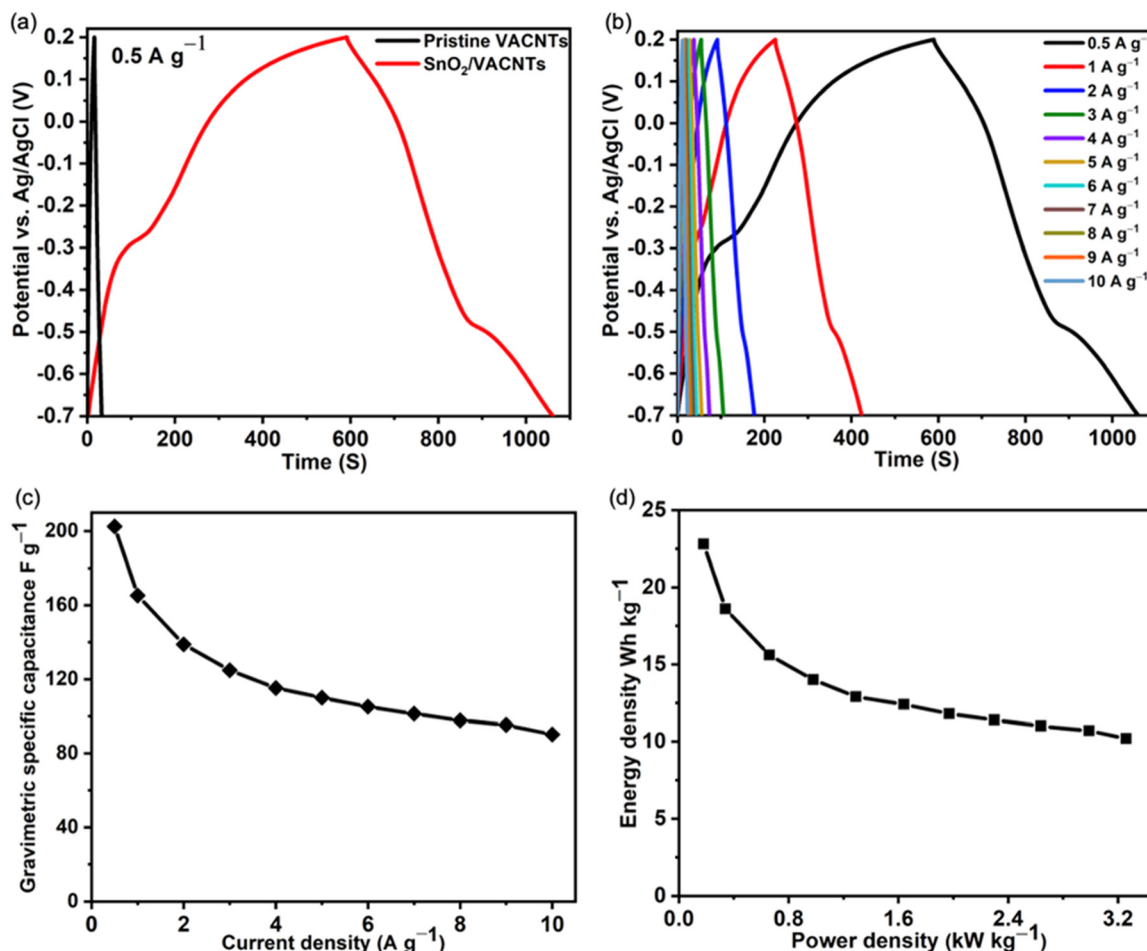


Fig. 4 (a) GCD curves of the pristine VACNTs and the SnO<sub>2</sub>/VACNTs electrodes at a constant current density of 0.5 A g<sup>-1</sup>. (b) GCD curves of the SnO<sub>2</sub>/VACNTs at different current densities. (c) Specific capacitance vs. current density graph of the SnO<sub>2</sub>/VACNTs electrode. (d) Ragone plot of the SnO<sub>2</sub>/VACNTs electrode.

using eqn (6), are 18.5 F g<sup>-1</sup> for pristine VACNTs and 202.56 F g<sup>-1</sup> for SnO<sub>2</sub>/VACNTs, demonstrating a substantial increase in charge storage due to the incorporation of SnO<sub>2</sub>. The prolonged discharge time for the SnO<sub>2</sub>/VACNTs highlights the contribution of redox reactions to the overall capacitance, significantly enhancing its energy storage capability. The gravimetric specific capacitance value of the pristine VACNTs electrode was calculated from the discharge curve using the equation below:<sup>94</sup>

$$C_{\text{grav}} = \frac{I\Delta t}{m\Delta V} \quad (6a)$$

where  $I$  (A) is the discharge current,  $m$  is the mass of the active materials in grams (g),  $\Delta t$  is the discharge time in seconds, and  $\Delta V$  is the discharge potential window in volts.

The gravimetric specific capacitance of the SnO<sub>2</sub>/VACNTs electrode at different current densities were calculated from the nonlinear GCD curves using the following equation:<sup>95</sup>

$$C_{\text{grav}} = 2I_m \frac{\int V dt}{(\Delta V)^2} \quad (6b)$$

where  $I_m$  is the current density in A g<sup>-1</sup>,  $\int V dt$  is the current integral area and,  $\Delta V$  is the discharge potential window in volts.

The charge–discharge profiles of SnO<sub>2</sub>/VACNTs at different current densities ranging from 0.5 A g<sup>-1</sup> to 10 A g<sup>-1</sup> are shown in Fig. 4(b). At lower current densities, the charge–discharge curves exhibit distinct voltage plateaus, further confirming the pseudocapacitive nature of the material. As the current density increases, the discharge time decreases due to ion diffusion limitations, restricting the full utilization of active sites. However, the SnO<sub>2</sub>/VACNTs electrode maintains a stable charge–discharge profile across all current densities, demonstrating excellent rate capability and structural integrity.

Fig. 4(c) illustrates the variation of gravimetric specific capacitance with current density. The gravimetric specific capacitance decreases from 202.56 F g<sup>-1</sup> at 0.5 A g<sup>-1</sup> to 90.22 F g<sup>-1</sup> at a high current density of 10 A g<sup>-1</sup>. The decline in specific capacitance as the current density increases is due to limited ion diffusion at higher charge–discharge rates.



Despite this, the SnO<sub>2</sub>/VACNTs composite retains a relatively high capacitance even at elevated current densities, indicating efficient ionic transport and excellent rate capability.

The Ragone plot of the composite electrode at different current densities is derived from the charge–discharge curves using the following equations and is presented in Fig. 4(d).

$$E (\text{Wh kg}^{-1}) = \frac{1}{2} \frac{C_{\text{sp}}(\Delta V)^2}{3.6} \quad (7)$$

$$P (\text{kW kg}^{-1}) = \frac{E \times 3.6}{\Delta t} \quad (8)$$

where  $E$ ,  $P$ ,  $C_{\text{sp}}$ ,  $\Delta V$ , and  $\Delta t$  denote the energy density (Wh kg<sup>-1</sup>), power density (kW kg<sup>-1</sup>), specific capacitance (F g<sup>-1</sup>), discharge potential window (V), and discharge time (seconds), respectively.

The SnO<sub>2</sub>/VACNTs electrode delivers a high energy density of 22.79 Wh kg<sup>-1</sup> at a power density of 0.18 kW kg<sup>-1</sup>, outperforming many SnO<sub>2</sub>-based hybrids, with reported energy density values between 10–21 Wh kg<sup>-1</sup>.<sup>80,96–99</sup>

However, as the power density increases to 3.26 kW kg<sup>-1</sup>, the energy density decreases to 10.15 Wh kg<sup>-1</sup>, a typical trend of supercapacitors. At lower power densities, the electrode can store more energy due to prolonged ion interaction times, while at higher power densities, rapid charge–discharge cycling reduces ion accessibility, limiting energy storage. Despite this, the SnO<sub>2</sub>/VACNTs composite retains a comparatively high energy density even at elevated power density. This performance is attributed to the highly conductive and porous VACNT framework, which supports efficient electron transport and rapid ion diffusion, as well as the SnO<sub>2</sub> nanoparticles, which contribute additional pseudocapacitive charge storage through reversible faradaic reactions.

Table 1 below compares the electrochemical performance obtained in this study with reported values from the literature using similar materials. As seen in the table, typical SnO<sub>2</sub> composites such as SnO<sub>2</sub>/C, SnO<sub>2</sub>/graphene, and SnO<sub>2</sub>/MWCNTs exhibit specific capacitances in the range of 37–184 F g<sup>-1</sup>, often limited by random carbon or CNTs orientations, binder interfaces, and sluggish ion transport. In contrast, the

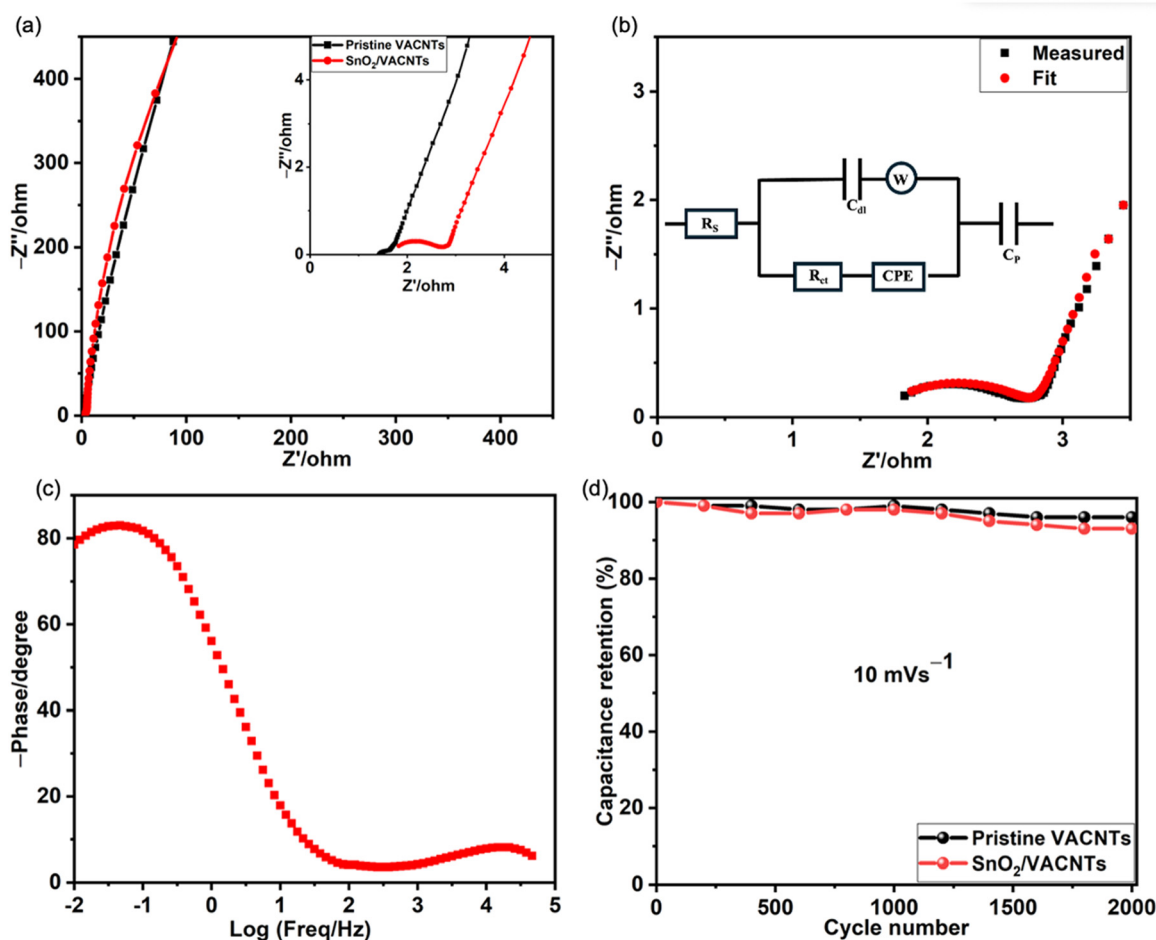


Fig. 5 (a) Nyquist plots of the pristine VACNTs and the SnO<sub>2</sub>/VACNTs electrodes (the inset shows the high-frequency region of the plots). (b) Nyquist plot of the SnO<sub>2</sub>/VACNTs electrode with equivalent-circuit fitting (inset shows the circuit model). (c) Bode plot of the SnO<sub>2</sub>/VACNTs electrode. (d) Cycling performance of the pristine VACNTs and the SnO<sub>2</sub>/VACNTs electrodes over 2000 cycles at a constant scan rate of 10 mV s<sup>-1</sup>.



SnO<sub>2</sub>/VACNTs architecture developed in this work provides a well-ordered, porous and interconnected framework that promotes rapid ion diffusion and efficient electrolyte access to the active sites. The vertical alignment of the CNTs ensures direct, continuous electron pathways from the current collector to the active surface, effectively reducing charge-transfer resistance and enhancing rate capability. Additionally, the direct growth of VACNTs on Ni foam eliminates polymeric binders and ensures strong electrical contact, while the conformal SnO<sub>2</sub> coating maximizes redox-active surface area and charge utilization. The combination of these structural and interfacial advantages explains the superior electrochemical performance observed in this study, confirming the distinct advantage of the SnO<sub>2</sub>/VACNTs composite over pristine VACNTs and other carbon-based SnO<sub>2</sub> composites reported in the literature (Table 1).

Fig. 5(a) shows the Nyquist plots of the pristine VACNTs and the SnO<sub>2</sub>/VACNTs electrodes, showing the frequency response of the electrode and electrolyte in terms of the real ( $Z'$ ) on the  $x$ -axis and imaginary ( $Z''$ ) on the  $y$ -axis. The series resistance ( $R_s$ ), which accounts for the electrode, electrode material, and contact resistance,<sup>106</sup> is 1.41  $\Omega$  for pristine VACNTs and 1.65  $\Omega$  for SnO<sub>2</sub>/VACNTs. The slight increase in  $R_s$  for SnO<sub>2</sub>/VACNTs is attributed to incorporating SnO<sub>2</sub> nanoparticles, which introduce additional resistance due to their semiconducting nature.<sup>107</sup> The charge transfer resistance ( $R_{ct}$ ), which represents the resistance at the electrode–electrolyte interface, is significantly lower for pristine VACNTs (0.23  $\Omega$ ) compared to SnO<sub>2</sub>/VACNTs (0.93  $\Omega$ ). The increased  $R_{ct}$  for SnO<sub>2</sub>/VACNTs suggests that introducing SnO<sub>2</sub> nanoparticles increases interfacial resistance due to redox reactions involved in pseudocapacitive charge storage. Nevertheless, the  $R_{ct}$  value obtained in this study remains significantly lower than those reported by Samuel *et al.*<sup>60</sup> for various SnO<sub>2</sub>/CNF composites, where  $R_{ct}$  values ranged from 2.97  $\Omega$  to 120.4  $\Omega$ . In this work, the highly conductive VACNTs network in the hybrid electrode helps to reduce the charge transfer resistance by providing rapid electron transport pathways. The low-frequency region of the Nyquist plot exhibits a nearly vertical slope corresponding to the Warburg impedance ( $W$ ).<sup>108</sup> The Warburg resistance arises from the interaction between electrolyte ions and the electrode surface, where the slope of the line represents how well ions penetrate the electrode structure.<sup>109</sup> The steep vertical nature of the slope in both pristine VACNTs and SnO<sub>2</sub>/VACNTs suggests efficient electrolyte ion transport and minimal ion-diffusion limitations within both electrodes. This excellent behavior is attributed to the well-aligned and porous VACNTs structure, which facilitates rapid ion movement. The inset of Fig. 5(a) focuses on the high-frequency region, where the semicircle represents the  $R_{ct}$ .<sup>110</sup> The noticeably larger semicircle for SnO<sub>2</sub>/VACNTs confirms the increased  $R_{ct}$  due to the faradaic reactions introduced by SnO<sub>2</sub>. Fig. 5(b) shows the Nyquist plot of the SnO<sub>2</sub>/VACNTs electrode together with the corresponding equivalent-circuit fit. The impedance

spectrum displays a distinct semicircle in the high- to mid-frequency region, followed by the characteristic inclined line associated with diffusion processes at lower frequencies. The excellent overlap between the measured data and the fitted curve demonstrates that the chosen circuit model (inset) accurately describes the electrode behavior. As shown, the model consists of  $R_s$ ,  $R_{ct}$ , double-layer capacitance ( $C_{dl}$ ) and a constant phase element (CPE) accounting for non-ideal capacitive behavior. A Warburg element ( $W$ ) captures ion diffusion within the porous electrode, and a pseudocapacitive element ( $C_p$ ) represents reversible faradaic storage at the electrode surface. Fig. 5(c) presents the corresponding Bode phase-angle plot. The phase angle ( $\alpha$ ) reaches  $\approx 83^\circ$  at low frequency (0.01 Hz), approaching the ideal  $90^\circ$  value expected for purely capacitive behavior.<sup>111</sup> This high phase angle confirms that the SnO<sub>2</sub>/VACNTs electrode exhibits predominantly capacitive behavior with negligible ion-diffusion limitations, consistent with the nearly vertical low-frequency region observed in the Nyquist plot.

Furthermore, Fig. 5(d) shows the capacitance of both electrodes over 2000 cycles at a constant scan rate of 10 mV s<sup>-1</sup>. Both electrodes demonstrate excellent electrochemical stability, with the pristine VACNTs electrode retaining 96% of its initial capacitance and the SnO<sub>2</sub>/VACNTs maintaining 93% after 2000 cycles. The high cycling stability of the SnO<sub>2</sub>/VACNTs electrode can be primarily attributed to the mechanically and electrically robust VACNT framework. The vertically aligned structure provides strong structural support that accommodates the strain and volume changes associated with the redox activity of SnO<sub>2</sub> during repeated cycling.<sup>112</sup> This buffering effect helps prevent nanoparticle agglomeration, detachment, or pulverization; degradation pathways commonly observed in metal oxide-based electrodes.<sup>113</sup> In addition, the continuous interconnected network of VACNTs offers highly conductive pathways for electron transport, ensuring consistent electrical connectivity throughout the electrode even as structural stresses accumulate during cycling.<sup>114</sup>

## 4. Conclusion

In this work, a hybrid SnO<sub>2</sub>/VACNTs electrode was successfully synthesized, exhibiting excellent electrochemical performance for supercapacitor applications. The aligned and porous structure of the VACNTs ensured rapid ion transport and enhanced charge transfer, while the pseudocapacitive SnO<sub>2</sub> nanoparticles significantly improved energy storage capacity. The composite electrode delivered a high gravimetric specific capacitance of 262.39 F g<sup>-1</sup> at 5 mV s<sup>-1</sup>, a high energy density of 22.79 W h kg<sup>-1</sup> at 0.18 kW kg<sup>-1</sup>, and excellent cycling stability with 93% capacitance retention over 2000 cycles. The integration of VACNTs and SnO<sub>2</sub> effectively combines electric double-layer capacitance (EDLC) with pseudocapacitive charge storage, reducing charge transfer resistance and improving rate performance. These



results position SnO<sub>2</sub>/VACNTs composites as strong candidates for next-generation energy storage devices and provide a scalable solution for high-power and high-energy-density supercapacitors.

## Author contributions

Chinaza E. Nwanno: conceptualization, methodology, investigation, data curation, writing – original draft, writing – review, and editing. Arun Thapa: investigation, data curation, writing – review, and editing. John Watt: investigation, discussion, writing – review, and editing. Winson Kuo: investigation, discussion, writing – review, and editing. Wenzhi Li: conceptualization, methodology, discussion, validation, funding acquisition, supervision, writing – review, and editing.

## Conflicts of interest

The authors do not have any conflicts of interest to declare.

## Data availability

The plots and figures in this manuscript reflect the original data. Raw data associated with the data presented in this work will be made available at reasonable request.

Supplementary information (SI) is available. See DOI: <https://doi.org/10.1039/d5lf00258c>.

## Acknowledgements

This work was supported by the National Science Foundation under grant 2213923. The authors would like to thank Dr. Prahald Siwakoti and Dr. Jiandi Zhang for their help with the XPS experiments. The authors would also like to acknowledge and appreciate the support from the Advanced Materials Engineering Research Institute (AMERI) at Florida International University. This work was performed, in part, at the Center for Integrated Nanotechnologies, an Office of Science User Facility operated for the U.S. Department of Energy (DOE) Office of Science. Los Alamos National Laboratory, an affirmative action-equal opportunity employer, is managed by Triad National Security, LLC for the U.S. Department of Energy's NNSA, under contract 89233218CNA000001.

## References

- Q. Sun, K. Li, T. Shu, Z. Guo, Y. Li and Y. Zhang, *et al.*, Mxene quantum dot insertion-induced electron transfer in CoFe LDH for high-performance zinc-air batteries, *Chem. Eng. J.*, 2025, **516**, 164075, DOI: [10.1016/j.ccej.2025.164075](https://doi.org/10.1016/j.ccej.2025.164075).
- T. Shu, X. Yang, Z. Huang, M. Qiao, J. Ning and K. Li, *et al.*, A hydrophobic phenolic polymer layer with high-flux Zn<sup>2+</sup>-specific regular channels for stabilizing aqueous zinc anodes, *J. Mater. Chem. A*, 2024, **12**(8), 4666–4677, DOI: [10.1039/D3TA06472G](https://doi.org/10.1039/D3TA06472G).
- C. E. Nwanno and W. Li, Aligned carbon nanotubes for lithium-ion batteries: A review, *Nano Res.*, 2023, **16**, 12384–12410, DOI: [10.1007/s12274-023-6006-2](https://doi.org/10.1007/s12274-023-6006-2).
- K. M. Liao, Y. K. Dai, H. Y. Wang, S. Deng and G. P. Dai, 3D Graphene Nanoflake/Vertically Aligned Carbon Nanotube/CoAl Layered Double Oxide Composites for High-Performance Lithium-Ion Batteries, *ACS Appl. Energy Mater.*, 2025, **8**(6), 3892–3903.
- H. Chen, X. Du, R. Wu, Y. Wang, J. Sun and Y. Zhang, *et al.*, Facile hydrothermal synthesis of porous MgCo<sub>2</sub>O<sub>4</sub> nanoflakes as an electrode material for high-performance asymmetric supercapacitors, *Nanoscale Adv.*, 2020, **2**(8), 3263–3275.
- E. Niknam, H. Naffakh-Moosavy, S. E. Moosavifard and M. G. Afshar, Multi-shelled bimetal V-doped Co<sub>3</sub>O<sub>4</sub> hollow spheres derived from metal organic framework for high performance supercapacitors, *J. Energy Storage*, 2021, **44**, 103508, DOI: [10.1016/j.est.2021.103508](https://doi.org/10.1016/j.est.2021.103508).
- X. Hu, Z. Deng, J. Suo and Z. Pan, A high rate, high capacity and long life (LiMn<sub>2</sub>O<sub>4</sub> + AC)/Li<sub>4</sub>Ti<sub>5</sub>O<sub>12</sub> hybrid battery-supercapacitor, *J. Power Sources*, 2009, **187**(2), 635–639.
- C. Portet, P. L. Taberna, P. Simon, E. Flahaut and C. Laberty-Robert, High power density electrodes for Carbon supercapacitor applications, *Electrochim. Acta*, 2005, **50**(20), 4174–4181.
- K. Li, Y. Xiao, T. Zheng, Q. Sun, Y. Zhang and H. Teng, *et al.*, Vanadium doping and phosphorus vacancy co-regulation of biotemplate derived three-dimensional cobalt phosphide to enhance pseudocapacitance performance, *Appl. Surf. Sci.*, 2023, **622**, 156950, DOI: [10.1016/j.apsusc.2023.156950](https://doi.org/10.1016/j.apsusc.2023.156950).
- N. C. Abeykoon, J. S. Bonso and J. P. Ferraris, Supercapacitor performance of carbon nanofiber electrodes derived from immiscible PAN/PMMA polymer blends, *RSC Adv.*, 2015, **5**(26), 19865–19873.
- X. Xu, J. Li, Y. Li, B. Ni, X. Liu and L. Pan, Selection of Carbon Electrode Materials, *Interface Sci. Technol.*, 2018, **24**, 65–83, DOI: [10.1016/B978-0-12-811370-7.00004-8](https://doi.org/10.1016/B978-0-12-811370-7.00004-8).
- J. Lück and A. Latz, Modeling of the electrochemical double layer and its impact on intercalation reactions, *Phys. Chem. Chem. Phys.*, 2018, **20**(44), 27804–27821.
- M. Favaro, B. Jeong, P. N. Ross, J. Yano, Z. Hussain and Z. Liu, *et al.*, Unravelling the electrochemical double layer by direct probing of the solid/liquid interface, *Nat. Commun.*, 2016, **7**, 1–8.
- Z. Z. Zhu, G. C. Wang, M. Q. Sun, X. W. Li and C. Z. Li, Fabrication and electrochemical characterization of polyaniline nanorods modified with sulfonated carbon nanotubes for supercapacitor applications, *Electrochim. Acta*, 2011, **56**(3), 1366–1372, DOI: [10.1016/j.electacta.2010.10.070](https://doi.org/10.1016/j.electacta.2010.10.070).
- P. Bhojane, Recent advances and fundamentals of Pseudocapacitors: Materials, mechanism, and its understanding, *J. Energy Storage*, 2022, **45**, 103654, DOI: [10.1016/j.est.2021.103654](https://doi.org/10.1016/j.est.2021.103654).
- N. R. Chodankar, H. D. Pham, A. K. Nanjundan, J. F. S. Fernando, K. Jayaramulu and D. Golberg, *et al.*, True



- Meaning of Pseudocapacitors and Their Performance Metrics: Asymmetric versus Hybrid Supercapacitors, *Small*, 2020, **16**(37), 1–35.
- 17 C. Costentin, T. R. Porter and J. M. Savéant, How Do Pseudocapacitors Store Energy? Theoretical Analysis and Experimental Illustration, *ACS Appl. Mater. Interfaces*, 2017, **9**(10), 8649–8658.
  - 18 J. Li, X. Wang, Z. Wu and J. Liu, *Electrochemical Energy Storage Technologies beyond Li-ion Batteries: Fundamentals, Materials, Devices*, Elsevier Inc., 2024.
  - 19 O. S. Okwundu, E. U. Aniekwe and C. E. Nwanno, Unlimited potentials of carbon: different structures and uses (a Review), *Metall. Mater. Eng.*, 2018, **24**(3), 145–171.
  - 20 J. Gamby, P. L. Taberna, P. Simon, J. F. Fauvarque and M. Chesneau, Studies and characterisations of various activated carbons used for carbon/carbon supercapacitors, *J. Power Sources*, 2001, **101**(1), 109–116.
  - 21 E. Frackowiak, Carbon materials for supercapacitor application, *Phys. Chem. Chem. Phys.*, 2007, **9**(15), 1774–1785.
  - 22 S. Aryal, K. R. Shrestha, T. Shrestha, H. B. Oli, I. Pathak and R. L. Shrestha, *et al.*, Activated carbon from *Prunus persica* seed stones as a negatrod material for high-performance supercapacitors, *J. Mol. Struct.*, 2025, **1323**, 140810, DOI: [10.1016/j.molstruc.2024.140810](https://doi.org/10.1016/j.molstruc.2024.140810).
  - 23 N. A. Saputra, G. Pari, W. Syafii, D. S. Nawawi, A. Maddu and N. Chitranningrum, *et al.*, Preparation and application of a novel supercapacitor from chemically activated red calliandra, *Mater. Chem. Phys.*, 2025, **329**, 130104, DOI: [10.1016/j.matchemphys.2024.130104](https://doi.org/10.1016/j.matchemphys.2024.130104).
  - 24 X. Liu, S. Li, R. Mi, J. Mei, L. M. Liu and L. Cao, *et al.*, Porous structure design of carbon xerogels for advanced supercapacitor, *Appl. Energy*, 2015, **153**, 32–40, DOI: [10.1016/j.apenergy.2015.01.141](https://doi.org/10.1016/j.apenergy.2015.01.141).
  - 25 S. Mezzavilla, C. Zanella, P. R. Aravind, C. Della Volpe and G. D. Sorarù, Carbon xerogels as electrodes for supercapacitors. The influence of the catalyst concentration on the microstructure and on the electrochemical properties, *J. Mater. Sci.*, 2012, **47**(20), 7175–7180.
  - 26 E. G. Calvo, F. Lufrano, P. Staiti, A. Brigandi, A. Arenillas and J. A. Menéndez, Optimizing the electrochemical performance of aqueous symmetric supercapacitors based on an activated carbon xerogel, *J. Power Sources*, 2013, **241**, 776–782, DOI: [10.1016/j.jpowsour.2013.03.065](https://doi.org/10.1016/j.jpowsour.2013.03.065).
  - 27 E. G. Calvo, N. Ferrera-Lorenzo, J. A. Menéndez and A. Arenillas, Microwave synthesis of micro-mesoporous activated carbon xerogels for high performance supercapacitors, *Microporous Mesoporous Mater.*, 2013, **168**, 206–212, DOI: [10.1016/j.micromeso.2012.10.008](https://doi.org/10.1016/j.micromeso.2012.10.008).
  - 28 R. Saliger, U. Fischer, C. Herta and J. Fricke, High surface area carbon aerogels for supercapacitors, *J. Non-Cryst. Solids*, 1998, **225**(1–3), 81–85.
  - 29 J. Li, X. Wang, Q. Huang, S. Gamboa and P. J. Sebastian, Studies on preparation and performances of carbon aerogel electrodes for the application of supercapacitor, *J. Power Sources*, 2006, **158**(1), 784–788.
  - 30 C. Zhao, H. Ou and C. Zhao, One-step preparation of waste epoxy resin-derived nanosized carbon aerogel and its high supercapacitor performance, *J. Energy Storage*, 2025, **106**, 114742, DOI: [10.1016/j.est.2024.114742](https://doi.org/10.1016/j.est.2024.114742).
  - 31 K. A. A. Abdou Elsehsah, Z. Ahmad Noorden and N. Mat Saman, Current insights and future prospects of graphene aerogel-enhanced supercapacitors: A systematic review, *Heliyon*, 2024, **10**(17), e37071, DOI: [10.1016/j.heliyon.2024.e37071](https://doi.org/10.1016/j.heliyon.2024.e37071).
  - 32 Y. Al Haj, A. B. Soliman, J. Vapaavuori and M. Elbahri, Carbon Aerogels Derived from Anion-Modified Nanocellulose for Adaptive Supercapacitor Performance, *Adv. Funct. Mater.*, 2024, **34**(28), 1–9.
  - 33 S. R. S. Prabaharan, R. Vimala and Z. Zainal, Nanostructured mesoporous carbon as electrodes for supercapacitors, *J. Power Sources*, 2006, **161**(1), 730–736.
  - 34 J. Zhao, C. Lai, Y. Dai and J. Xie, Pore structure control of mesoporous carbon as supercapacitor material, *Mater. Lett.*, 2007, **61**(23–24), 4639–4642.
  - 35 D. Saha, Y. Li, Z. Bi, J. Chen, J. K. Keum and D. K. Hensley, *et al.*, Studies on supercapacitor electrode material from activated lignin-derived mesoporous carbon, *Langmuir*, 2014, **30**(3), 900–910.
  - 36 F. Lufrano and P. Staiti, Mesoporous carbon materials as electrodes for electrochemical supercapacitors, *Int. J. Electrochem. Sci.*, 2010, **5**(6), 903–916, DOI: [10.1016/S1452-3981\(23\)15331-4](https://doi.org/10.1016/S1452-3981(23)15331-4).
  - 37 H. Liu, L. Feng, S. Zhu, Y. Chang, Y. Li and W. Hou, *et al.*, Synthesizing mesoporous carbon with small pore size, narrow distribution and enhanced capacitive performance, *J. Energy Storage*, 2025(112), 115576, DOI: [10.1016/j.est.2025.115576](https://doi.org/10.1016/j.est.2025.115576).
  - 38 H. Pan, J. Li and Y. P. Feng, Carbon nanotubes for supercapacitor, *Nanoscale Res. Lett.*, 2010, **5**(3), 654–668.
  - 39 Z. Yang, J. Tian, Z. Yin, C. Cui, W. Qian and F. Wei, Carbon nanotube- and graphene-based nanomaterials and applications in high-voltage supercapacitor: A review, *Carbon*, 2019, **141**, 467–480, DOI: [10.1016/j.carbon.2018.10.010](https://doi.org/10.1016/j.carbon.2018.10.010).
  - 40 E. Frackowiak, K. Metenier, V. Bertagna and F. Beguin, Supercapacitor electrodes from multiwalled carbon nanotubes, *Appl. Phys. Lett.*, 2000, **77**(15), 2421–2423.
  - 41 R. Isci, K. B. Donmez, N. Karatepe and T. Ozturk, High-Performance Thienothiophene and Single Wall Carbon Nanotube-Based Supercapacitor as a Free-Standing and Flexible Hybrid Energy Storage Material, *ACS Appl. Energy Mater.*, 2024, **7**(4), 1488–1494.
  - 42 V. V. N. Obreja, On the performance of supercapacitors with electrodes based on carbon nanotubes and carbon activated material-A review, *Phys. E*, 2008, **40**(7), 2596–2605.
  - 43 Y. Wang, Z. Shi, Y. Huang, Y. Ma, C. Wang and M. Chen, *et al.*, Supercapacitor devices based on graphene materials, *J. Phys. Chem. C*, 2009, **113**(30), 13103–13107.
  - 44 C. Liu, Z. Yu, D. Neff, A. Zhamu and B. Z. Jang, Graphene-based supercapacitor with an ultrahigh energy density, *Nano Lett.*, 2010, **10**(12), 4863–4868.



- 45 T. Y. Bin and J. M. Lee, Graphene for supercapacitor applications, *J. Mater. Chem. A*, 2013, **1**(47), 14814–14843.
- 46 W. Yang, M. Ni, X. Ren, Y. Tian, N. Li and Y. Su, *et al.*, Graphene in Supercapacitor Applications, *Curr. Opin. Colloid Interface Sci.*, 2015, **20**(5–6), 416–428, DOI: [10.1016/j.cocis.2015.10.009](https://doi.org/10.1016/j.cocis.2015.10.009).
- 47 Q. Ke and J. Wang, Graphene-based materials for supercapacitor electrodes – A review, *J. Mater.*, 2016, **2**(1), 37–54, DOI: [10.1016/j.jmat.2016.01.001](https://doi.org/10.1016/j.jmat.2016.01.001).
- 48 Q. Li, H. Zheng, B. Liu, T. Jian, W. Ma and C. Xu, *et al.*, One-Step Scalable Fabrication of Nitrogen and Chlorine Co-doped Graphene by Electrochemical Exfoliation for High-Performance Supercapacitors, *Trans. Tianjin Univ.*, 2024, **30**, 448–458, DOI: [10.1007/s12209-024-00412-2](https://doi.org/10.1007/s12209-024-00412-2).
- 49 C. E. Nwanno, A. Thapa, J. Watt, D. Simkins Bendayan and W. Li, Field Emission Properties of Cu-Filled Vertically Aligned Carbon Nanotubes Grown Directly on Thin Cu Foils, *Nanomaterials*, 2024, **14**(11), 988, DOI: [10.3390/nano14110988](https://doi.org/10.3390/nano14110988).
- 50 A. G. Olabi, Q. Abbas, M. A. Abdelkareem, A. H. Alami, M. Mirzaeian and E. T. Sayed, Carbon-Based Materials for Supercapacitors: Recent Progress, Challenges and Barriers, *Batteries*, 2023, **9**(1), 19, DOI: [10.3390/batteries9010019](https://doi.org/10.3390/batteries9010019).
- 51 W. Lu, L. Qu, K. Henry and L. Dai, High performance electrochemical capacitors from aligned carbon nanotube electrodes and ionic liquid electrolytes, *J. Power Sources*, 2009, **189**(2), 1270–1277.
- 52 R. Reit, J. Nguyen and W. J. Ready, Growth time performance dependence of vertically aligned carbon nanotube supercapacitors grown on aluminum substrates, *Electrochim. Acta*, 2013, **91**, 96–100, DOI: [10.1016/j.electacta.2012.12.058](https://doi.org/10.1016/j.electacta.2012.12.058).
- 53 V. Ghai, K. Chatterjee and P. K. Agnihotri, Vertically aligned carbon nanotubes-coated aluminium foil as flexible supercapacitor electrode for high power applications, *Carbon Lett.*, 2021, **31**(3), 473–481, DOI: [10.1007/s42823-020-00176-4](https://doi.org/10.1007/s42823-020-00176-4).
- 54 H. A. Moreno, S. Hussain, R. Amade and E. Bertran, Growth and functionalization of CNTs on stainless steel electrodes for supercapacitor applications, *Mater. Res. Express*, 2014, **1**(3), 35050, DOI: [10.1088/2053-1591/1/3/035050](https://doi.org/10.1088/2053-1591/1/3/035050).
- 55 Y. Zou, I. A. Kinloch and R. A. W. Dryfe, Mesoporous Vertical Co<sub>3</sub>O<sub>4</sub> Nanosheet Arrays on Nitrogen-Doped Graphene Foam with Enhanced Charge-Storage Performance, *ACS Appl. Mater. Interfaces*, 2015, **7**(41), 22831–22838.
- 56 A. Singh and A. Chandra, Enhancing specific energy and power in asymmetric supercapacitors – A synergetic strategy based on the use of redox additive electrolytes, *Sci. Rep.*, 2016, **6**, 1–13.
- 57 Z. J. Li, T. X. Chang, G. Q. Yun and Y. Jia, Coating single walled carbon nanotube with SnO<sub>2</sub> and its electrochemical properties, *Powder Technol.*, 2012, **224**, 306–310.
- 58 V. Vinoth, J. J. Wu, A. M. Asiri, T. Lana-Villarreal, P. Bonete and S. Anandan, SnO<sub>2</sub>-decorated multiwalled carbon nanotubes and Vulcan carbon through a sonochemical approach for supercapacitor applications, *Ultrason. Sonochem.*, 2016, **29**, 205–212, DOI: [10.1016/j.ultsonch.2015.09.013](https://doi.org/10.1016/j.ultsonch.2015.09.013).
- 59 F. H. Kuok, C. Y. Liao, C. W. Chen, Y. C. Hao, I. S. Yu and J. Z. Chen, Screen-printed SnO<sub>2</sub>/CNT quasi-solid-state gel-electrolyte supercapacitor, *Mater. Res. Express.*, 2017, **4**, 115501, DOI: [10.1088/2053-1591/aa9405](https://doi.org/10.1088/2053-1591/aa9405).
- 60 E. Samuel, B. Joshi, H. S. Jo, K. Y. Il, M. T. Swihart and J. M. Yun, *et al.*, Flexible and freestanding core-shell SnOx/carbon nanofiber mats for high-performance supercapacitors, *J. Alloys Compd.*, 2017, **728**, 1362–1371, DOI: [10.1016/j.jallcom.2017.09.103](https://doi.org/10.1016/j.jallcom.2017.09.103).
- 61 S. P. Lim, N. M. Huang and H. N. Lim, Solvothermal synthesis of SnO<sub>2</sub>/graphene nanocomposites for supercapacitor application, *Ceram. Int.*, 2013, **39**(6), 6647–6655, DOI: [10.1016/j.ceramint.2013.01.102](https://doi.org/10.1016/j.ceramint.2013.01.102).
- 62 A. Thapa, A. R. Baboukani, P. Siwakoti, K. L. Jungjohann, C. E. Nwanno and J. Zhang, *et al.*, Binder-free tin (IV) oxide coated vertically aligned carbon nanotubes as anode for lithium-ion batteries, *J. Power Sources*, 2025(625), 235697, DOI: [10.1016/j.jpowsour.2024.235697](https://doi.org/10.1016/j.jpowsour.2024.235697).
- 63 S. Santangelo, Controlled surface functionalization of carbon nanotubes by nitric acid vapors generated from sub-azeotropic solution, *Surf. Interface Anal.*, 2016, **48**(1), 17–25.
- 64 E. B. Barros, A. G. S. Filho, V. Lemos, J. M. Filho, S. B. Fagan and M. H. Herbst, *et al.*, Charge transfer effects in acid treated single-wall carbon nanotubes, *Carbon*, 2005, **43**(12), 2495–2500.
- 65 W. Fan, L. Gao and J. Sun, Tin oxide nanoparticle-functionalized multi-walled carbon nanotubes by the vapor phase method, *J. Am. Ceram. Soc.*, 2006, **89**(8), 2671–2673.
- 66 Z. Wang, G. Chen and D. Xia, Coating of multi-walled carbon nanotube with SnO<sub>2</sub> films of controlled thickness and its application for Li-ion battery, *J. Power Sources*, 2008, **184**(2), 432–436.
- 67 A. Thapa, K. L. Jungjohann, X. Wang and W. Li, Improving field emission properties of vertically aligned carbon nanotube arrays through a structure modification, *J. Mater. Sci.*, 2020, **55**(5), 2101–2117, DOI: [10.1007/s10853-019-04156-6](https://doi.org/10.1007/s10853-019-04156-6).
- 68 S. Murata, M. Imanishi, S. Hasegawa and R. Namba, Vertically aligned carbon nanotube electrodes for high current density operating proton exchange membrane fuel cells, *J. Power Sources*, 2014, **253**, 90–97, DOI: [10.1016/j.jpowsour.2013.11.073](https://doi.org/10.1016/j.jpowsour.2013.11.073).
- 69 P. Lv, P. Zhang, F. Li, Y. Li, Y. Feng and W. Feng, Vertically aligned carbon nanotubes grown on carbon fabric with high rate capability for super-capacitors, *Synth. Met.*, 2012, **162**(13–14), 1090–1096.
- 70 Y. Li and M. Kröger, A theoretical evaluation of the effects of carbon nanotube entanglement and bundling on the structural and mechanical properties of buckypaper, *Carbon*, 2012, **50**(5), 1793–1806.
- 71 A. Mashayekhi, S. M. Hosseini, M. Hassanpour Amiri, N. Namdar and Z. Sanaee, Plasma-assisted nitrogen doping of VACNTs for efficiently enhancing the supercapacitor performance, *J. Nanopart. Res.*, 2016, **18**(6), 1–15.



- 72 A. Kis, G. Csányi, J. P. Salvetat, T. N. Lee, E. Couteau and A. J. Kulik, *et al.*, Reinforcement of single-walled carbon nanotube bundles by intertube bridging, *Nat. Mater.*, 2004, **3**(3), 153–157.
- 73 X. Zhang, W. Lu, G. Zhou and Q. Li, Understanding the Mechanical and Conductive Properties of Carbon Nanotube Fibers for Smart Electronics, *Adv. Mater.*, 2020, **32**(5), 1–21.
- 74 H. Wang, Y. Wang, Z. Hu and X. Wang, Cutting and unzipping multiwalled carbon nanotubes into curved graphene nanosheets and their enhanced supercapacitor performance, *ACS Appl. Mater. Interfaces*, 2012, **4**(12), 6827–6834.
- 75 K. R. Hallam, J. E. Darnbrough, C. Paraskevoulakos, P. J. Heard, T. J. Marrow and P. E. J. Flewitt, Measurements by x-ray diffraction of the temperature dependence of lattice parameter and crystallite size for isostatically-pressed graphite, *Carbon Trends*, 2021, **4**, 100071, DOI: [10.1016/j.cartre.2021.100071](https://doi.org/10.1016/j.cartre.2021.100071).
- 76 W. S. K. Bong, A. Shiota, T. Miwa, Y. Morino, S. Kanada and K. Kawamoto, Effect of thickness and uniformity of LiNbO<sub>3</sub>-coated layer on LiNi<sub>0.5</sub>Co<sub>0.2</sub>Mn<sub>0.3</sub>O<sub>2</sub> cathode material on enhancement of cycle performance of full-cell sulfide-based all-solid-state batteries, *J. Power Sources*, 2023, **577**, 233259, DOI: [10.1016/j.jpowsour.2023.233259](https://doi.org/10.1016/j.jpowsour.2023.233259).
- 77 K. S. Lee, M. Park, J. M. Ko and J. D. Kim, Electrochemical properties of multi-walled carbon nanotubes treated with nitric acid for a supercapacitor electrode, *Colloids Surf., A*, 2016, **506**, 664–669, DOI: [10.1016/j.colsurfa.2016.07.044](https://doi.org/10.1016/j.colsurfa.2016.07.044).
- 78 R. A. Fisher, M. R. Watt and R. W. Jud, Functionalized Carbon Nanotube Supercapacitor Electrodes: A Review on Pseudocapacitive Materials, *ECS J. Solid State Sci. Technol.*, 2013, **2**(10), M3170–M3177.
- 79 X. He, G. Liu, B. Yan, H. Suo and C. Zhao, Significant enhancement of electrochemical behaviour by incorporation of carboxyl group functionalized carbon nanotubes into polyaniline based supercapacitor, *Eur. Polym. J.*, 2016, **83**, 53–59, DOI: [10.1016/j.eurpolymj.2016.08.001](https://doi.org/10.1016/j.eurpolymj.2016.08.001).
- 80 Y. Luan, G. Nie, X. Zhao, N. Qiao, X. Liu and H. Wang, *et al.*, The integration of SnO<sub>2</sub> dots and porous carbon nanofibers for flexible supercapacitors, *Electrochim. Acta*, 2019, **308**, 121–130.
- 81 J. Mu, B. Chen, Z. Guo, M. Zhang, Z. Zhang and C. Shao, *et al.*, Tin oxide (SnO<sub>2</sub>) nanoparticles/electrospun carbon nanofibers (CNFs) heterostructures: Controlled fabrication and high capacitive behavior, *J. Colloid Interface Sci.*, 2011, **356**(2), 706–712, DOI: [10.1016/j.jcis.2011.01.032](https://doi.org/10.1016/j.jcis.2011.01.032).
- 82 B. Huang, J. Yang, Y. Zou, L. Ma and X. Zhou, Sonochemical synthesis of SnO<sub>2</sub>/carbon nanotubes encapsulated in graphene sheets composites for lithium ion batteries with superior electrochemical performance, *Electrochim. Acta*, 2014, **143**, 63–69, DOI: [10.1016/j.electacta.2014.07.119](https://doi.org/10.1016/j.electacta.2014.07.119).
- 83 B. Zhou, S. Yang, L. Wu, W. Wu, W. Wei and L. Chen, *et al.*, Amorphous carbon framework stabilized SnO<sub>2</sub> porous nanowires as high performance Li-ion battery anode materials, *RSC Adv.*, 2015, **5**(62), 49926–49932, DOI: [10.1039/C5RA05372B](https://doi.org/10.1039/C5RA05372B).
- 84 R. K. Selvan, I. Perelshtein, N. Perkas and A. Gedanken, Synthesis of hexagonal-shaped SnO<sub>2</sub> nanocrystals and SnO<sub>2</sub>@C nanocomposites for electrochemical redox supercapacitors, *J. Phys. Chem. C*, 2008, **112**(6), 1825–1830.
- 85 Y. Yang, S. Ren, X. Song, Y. Guo, D. Si and H. Jing, *et al.*, Sn@SnO<sub>2</sub> attached on carbon spheres as additive-free electrode for high-performance pseudocapacitor, *Electrochim. Acta*, 2016, **209**, 350–359, DOI: [10.1016/j.electacta.2016.05.105](https://doi.org/10.1016/j.electacta.2016.05.105).
- 86 V. Velmurugan, U. Srinivasarao, R. Ramachandran, M. Saranya and A. N. Grace, Synthesis of tin oxide/graphene (SnO<sub>2</sub>/G) nanocomposite and its electrochemical properties for supercapacitor applications, *Mater. Res. Bull.*, 2016, **84**, 145–151, DOI: [10.1016/j.materresbull.2016.07.015](https://doi.org/10.1016/j.materresbull.2016.07.015).
- 87 A. Priyadharsini, M. Saravanakumar, A. Sakunthala, A. Banu, J. Suryakanth and S. Pavithra, *et al.*, Role of preparation conditions on the pseudocapacitor properties of SnO<sub>2</sub> nanoparticles by co-precipitation method, *J. Mater. Sci.:Mater. Electron.*, 2024, **35**(6), 1–15, DOI: [10.1007/s10854-024-12239-7](https://doi.org/10.1007/s10854-024-12239-7).
- 88 M. Saghafi, F. Mahboubi, S. Mohajerzadeh and R. Holze, Preparation of vertically aligned carbon nanotubes and their electrochemical performance in supercapacitors, *Synth. Met.*, 2014, **195**, 252–259.
- 89 R. Amade, E. Jover, B. Caglar, T. Mutlu and E. Bertran, Optimization of MnO<sub>2</sub>/vertically aligned carbon nanotube composite for supercapacitor application, *J. Power Sources*, 2011, **196**(13), 5779–5783, DOI: [10.1016/j.jpowsour.2011.02.029](https://doi.org/10.1016/j.jpowsour.2011.02.029).
- 90 T. P. Gujar, W. Y. Kim, I. Puspitasari, K. D. Jung and O. S. Joo, Electrochemically deposited nanograin ruthenium oxide as a pseudocapacitive electrode, *Int. J. Electrochem. Sci.*, 2007, **2**(9), 666–673, DOI: [10.1016/S1452-3981\(23\)17102-1](https://doi.org/10.1016/S1452-3981(23)17102-1).
- 91 S. Ren, Y. Yang, M. Xu, H. Cai, C. Hao and X. Wang, Hollow SnO<sub>2</sub> microspheres and their carbon-coated composites for supercapacitors, *Colloids Surf., A*, 2014, **444**, 26–32, DOI: [10.1016/j.colsurfa.2013.12.028](https://doi.org/10.1016/j.colsurfa.2013.12.028).
- 92 T. S. Mathis, N. Kurra, X. Wang, D. Pinto, P. Simon and Y. Gogotsi, Energy Storage Data Reporting in Perspective—Guidelines for Interpreting the Performance of Electrochemical Energy Storage Systems, *Adv. Energy Mater.*, 2019, **9**(39), 1–13.
- 93 K. Li, Y. Xiao, T. Zheng, Q. Sun, Y. Zhang and H. Teng, *et al.*, Applied Surface Science Vanadium doping and phosphorus vacancy co-regulation of biotemplate derived three-dimensional cobalt phosphide to enhance pseudocapacitance performance, *Appl. Surf. Sci.*, 2023, **622**, 156950, DOI: [10.1016/j.apsusc.2023.156950](https://doi.org/10.1016/j.apsusc.2023.156950).
- 94 M. M. Huq, H. C. Te and C. Y. Ho, Preparation of carbon nanotube-activated carbon hybrid electrodes by electrophoretic deposition for supercapacitor applications, *Diamond Relat. Mater.*, 2016, **62**, 58–64, DOI: [10.1016/j.diamond.2015.12.014](https://doi.org/10.1016/j.diamond.2015.12.014).



- 95 L. Q. Mai, A. Minhas-khan, X. Tian, K. M. Hercule, Y. L. Zhao and X. Lin, Synergistic interaction between redox-active electrolyte and binder-free functionalized carbon for ultrahigh supercapacitor performance, *Nat. Commun.*, 2013, **4**, 2923, DOI: [10.1038/ncomms3923](https://doi.org/10.1038/ncomms3923).
- 96 J. Ge, Y. Qu, L. Cao, F. Wang, L. Dou and J. Yu, *et al.*, Polybenzoxazine-based highly porous carbon nanofibrous membranes hybridized by tin oxide nanoclusters: Durable mechanical elasticity and capacitive performance, *J. Mater. Chem. A*, 2016, **4**(20), 7795–7804.
- 97 R. Rani, M. Sharma, B. Mohan, A. Kumar, R. Chandra and V. K. Malik, Enhanced supercapacitive performance in catalyst-free binary composite SnO<sub>2</sub>-RuO<sub>2</sub> nanostructured thin films for symmetric supercapacitor device, *Energy Technol.*, 2024, **12**(7), 2301511, DOI: [10.1002/ente.202301511](https://doi.org/10.1002/ente.202301511).
- 98 A. B. Rohom, P. U. Londhe, J. In and N. B. Chauré, Conducting polymer wrapped SnO<sub>2</sub>/RGO nanocomposite: An efficient high-performance supercapacitor material, *Surf. Interfaces*, 2024(44), 103605, DOI: [10.1016/j.surfin.2023.103605](https://doi.org/10.1016/j.surfin.2023.103605).
- 99 T. Ahmad and M. Z. Ansari, Temperature-dependent structural and optical properties of Sb-doped SnO<sub>2</sub> nanoparticles and their electrochemical analysis for supercapacitor application, *New J. Chem.*, 2024, **48**(18), 8495–8509, DOI: [10.1039/D4NJ00918E](https://doi.org/10.1039/D4NJ00918E).
- 100 K. Komatsubara, H. Suzuki, H. Inoue, M. Kishibuchi, S. Takahashi and T. Marui, *et al.*, Highly Oriented Carbon Nanotube Supercapacitors, *ACS Appl. Nano Mater.*, 2022, **5**(1), 1521–1532.
- 101 Z. Yang, J. Deng, X. Chen, J. Ren and H. Peng, A highly stretchable, fiber-shaped supercapacitor, *Angew. Chem., Int. Ed.*, 2013, **52**(50), 13453–13457.
- 102 V. Naresh and S. K. Martha, Carbon Coated SnO<sub>2</sub> as a Negative Electrode Additive for High Performance Lead Acid Batteries and Supercapacitors, *J. Electrochem. Soc.*, 2019, **166**(4), A551–A558.
- 103 S. W. Hwang and S. H. Hyun, Synthesis and characterization of tin oxide/carbon aerogel composite electrodes for electrochemical supercapacitors, *J. Power Sources*, 2007, **172**(1), 451–459.
- 104 J. Li, X. Zhang, J. Guo, R. Peng, R. Xie and Y. Huang, *et al.*, Facile surfactant- and template-free synthesis and electrochemical properties of SnO<sub>2</sub>/graphene composites, *J. Alloys Compd.*, 2016, **674**, 44–50, DOI: [10.1016/j.jallcom.2016.02.212](https://doi.org/10.1016/j.jallcom.2016.02.212).
- 105 C. M. Chen, Q. Zhang, J. Q. Huang, W. Zhang, X. C. Zhao and C. H. Huang, *et al.*, Chemically derived graphene-metal oxide hybrids as electrodes for electrochemical energy storage: Pre-graphenization or post-graphenization?, *J. Mater. Chem.*, 2012, **22**(28), 13947–13955.
- 106 A. Celzard, F. Collas, J. F. Maréché, G. Furdin and I. Rey, Porous electrodes-based double-layer supercapacitors: Pore structure versus series resistance, *J. Power Sources*, 2002, **108**(1–2), 153–162.
- 107 S. Das and V. Jayaraman, SnO<sub>2</sub>: A comprehensive review on structures and gas sensors, *Prog. Mater. Sci.*, 2014, **66**, 112–255.
- 108 A. A. Moya, Low-frequency development approximations to the transmissive Warburg diffusion impedance, *J. Energy Storage*, 2022, **55**, 105632, DOI: [10.1016/j.est.2022.105632](https://doi.org/10.1016/j.est.2022.105632).
- 109 N. O. Laschuk, E. B. Easton and O. V. Zenkina, Reducing the resistance for the use of electrochemical impedance spectroscopy analysis in materials chemistry, *RSC Adv.*, 2021, **11**(45), 27925–27936.
- 110 A. Allison and H. A. Andreas, Minimizing the Nyquist-plot semi-circle of pseudocapacitive manganese oxides through modification of the oxide-substrate interface resistance, *J. Power Sources*, 2019, **426**, 93–96, DOI: [10.1016/j.jpowsour.2019.04.029](https://doi.org/10.1016/j.jpowsour.2019.04.029).
- 111 S. A. Pande, B. Pandit and B. R. Sankapal, Electrochemical approach of chemically synthesized HgS nanoparticles as supercapacitor electrode, *Mater. Lett.*, 2017, **209**, 97–101, DOI: [10.1016/j.matlet.2017.07.084](https://doi.org/10.1016/j.matlet.2017.07.084).
- 112 M. Aadil, S. Zulfiqar, M. Shahid, P. O. Agboola, S. Haider and M. F. Warsi, *et al.*, Fabrication of rationally designed CNTs supported binary nanohybrid with multiple approaches to boost electrochemical performance, *J. Electroanal. Chem.*, 2021, **884**, 115070, DOI: [10.1016/j.jelechem.2021.115070](https://doi.org/10.1016/j.jelechem.2021.115070).
- 113 M. Zhi, C. Xiang, J. Li, M. Li and N. Wu, Nanostructured carbon-metal oxide composite electrodes for supercapacitors: A review, *Nanoscale*, 2013, **5**, 72–88.
- 114 H. Sabeeh, M. Aadil, S. Zulfiqar, I. Ayeman, I. Shakir and P. O. Agboola, *et al.*, Self-Supporting Design of NiS/CNTs Nanohybrid for Advanced Electrochemical Energy Storage Applications, *J. Cluster Sci.*, 2022, **33**(5), 2113–2121, DOI: [10.1007/s10876-021-02138-w](https://doi.org/10.1007/s10876-021-02138-w).
- 115 M. U. Rani, V. Naresh, D. Damodar, S. Muduli, S. K. Martha and A. S. Deshpande, In-situ formation of mesoporous SnO<sub>2</sub>@C nanocomposite electrode for supercapacitors, *Electrochim. Acta*, 2021, **365**, 137284, DOI: [10.1016/j.electacta.2020.137284](https://doi.org/10.1016/j.electacta.2020.137284).
- 116 Y. Jin and M. Jia, Design and synthesis of nanostructured graphene-SnO<sub>2</sub>-polyaniline ternary composite and their excellent supercapacitor performance, *Colloids Surf., A*, 2015, **464**, 17–25, DOI: [10.1016/j.colsurfa.2014.09.032](https://doi.org/10.1016/j.colsurfa.2014.09.032).

